

Estimation of Size and Rotations of Icebergs from Historical Data Utilizing Scatterometer Data

Jeffrey Scott Budge

A thesis submitted to the faculty of  
Brigham Young University  
in partial fulfillment of the requirements for the degree of  
Master of Science

David G. Long, Chair  
Doran Wilde  
Daniel Smalley

Department of Electrical and Computer Engineering  
Brigham Young University

Copyright © 2017 Jeffrey Scott Budge

All Rights Reserved

## ABSTRACT

### Estimation of Size and Rotations of Icebergs from Historical Data Utilizing Scatterometer Data

Jeffrey Scott Budge

Department of Electrical and Computer Engineering, BYU

Master of Science

In this thesis, the development and methodology of a new, consolidated BYU/NIC Antarctic Iceberg Tracking Database is presented. The new database combines data from the original BYU daily iceberg tracking database derived from scatterometers, and the National Ice Center's weekly Antarctic iceberg tracking database derived from mostly optical and infrared sensors. Using this data, interpolation methods and statistical analyses of iceberg locations are discussed. The intent of this database is to consolidate iceberg location data in order to increase accessibility to users.

Active microwave remote sensing instruments are used to track tabular icebergs and provide a daily estimate of their positions and sizes. A consolidated data set of these positions from several different instruments is valuable to ensure accurate positional data. The scatterometer iceberg positional record began with the Seasat-A Satellite Scatterometer (SASS) and is continued with the Quick Scatterometer (QuikSCAT) and Advanced Scatterometer (ASCAT) data sets.

A reliable method of automatically estimating Antarctic iceberg contours and sizes from satellite data is desirable to help better understand patterns in iceberg formation and behavior. Starting from scatterometer images, this thesis develops a method of using the relatively constant backscatter values across the surface of an iceberg to derive a contour of its shape. Contours are then used to find an angle of rotation between images taken on successive days. This method produces size estimates that are within 10% of the area given by the National Ice Center (NIC). The size estimates and rotation angles are included in the new consolidated database.

Keywords: remote sensing, sea ice, OSCAT, ASCAT, iceberg, rotation, size

## ACKNOWLEDGMENTS

I would like to first and foremost thank Dr. Long for his many hours of instruction, assistance, correction, and patience. I would also like to thank my committee who reviewed my research. Many thanks go to the members of the MERS lab, past and present, who helped me along the way.

## TABLE OF CONTENTS

<b>LIST OF FIGURES</b> . . . . .	<b>iv</b>
<b>Chapter 1 Introduction</b> . . . . .	<b>1</b>
1.1 Thesis Statement . . . . .	2
1.2 Research Contributions . . . . .	3
1.3 Thesis Outline . . . . .	3
<b>Chapter 2 Background</b> . . . . .	<b>4</b>
2.1 Active Microwave Remote Sensing . . . . .	4
2.1.1 QuikSCAT . . . . .	4
2.1.2 ASCAT . . . . .	5
2.2 Scatterometer Backscatter Measurements . . . . .	6
2.3 Iceberg Tracking Methodology . . . . .	7
<b>Chapter 3 Database Implementation</b> . . . . .	<b>9</b>
3.1 Motivation . . . . .	9
3.2 Data Collection . . . . .	11
3.2.1 BYU MERS Data Collection . . . . .	11
3.2.2 NIC Data Collection . . . . .	12
3.3 Data Interpolation and Processing . . . . .	13
3.4 Summary . . . . .	16
<b>Chapter 4 Size Estimates</b> . . . . .	<b>18</b>
4.1 Introduction . . . . .	18
4.2 Windowing . . . . .	19
4.3 Mapping . . . . .	19
4.4 Adaptive Threshold . . . . .	20
4.5 Contour Estimation . . . . .	21
4.5.1 Apodization Window . . . . .	23
4.5.2 Noise Filtering . . . . .	24
4.6 Verification . . . . .	24
4.7 Summary . . . . .	25
<b>Chapter 5 Rotation Estimates</b> . . . . .	<b>27</b>
5.1 Introduction . . . . .	27
5.2 Ellipse Fitting . . . . .	27
5.3 Angle Estimation . . . . .	28
5.3.1 Error Bounds . . . . .	30
5.4 Summary . . . . .	31
<b>Chapter 6 Conclusion</b> . . . . .	<b>34</b>
6.1 Summary . . . . .	34

6.2	Future Work . . . . .	35
6.2.1	Melt Event Mitigation . . . . .	35
6.2.2	Automatic Iceberg Location . . . . .	35
6.2.3	Iceberg Location Prediction . . . . .	35
<b>REFERENCES . . . . .</b>		<b>36</b>
<b>Appendix A Database File Format Documentation . . . . .</b>		<b>38</b>
A.1	Introduction . . . . .	38
A.2	Structure . . . . .	38
A.3	Format . . . . .	38
A.3.1	Sensors . . . . .	39
A.3.2	date . . . . .	39
A.3.3	size_1 . . . . .	39
A.3.4	size_2 . . . . .	39
A.3.5	area . . . . .	39
A.3.6	date_gap . . . . .	40
A.3.7	disp . . . . .	40
A.3.8	flags . . . . .	40
A.3.9	lat . . . . .	40
A.3.10	lon . . . . .	40
A.3.11	mask . . . . .	41
A.3.12	rotation . . . . .	41

## LIST OF FIGURES

2.1	QuikSCAT scanning geometry [1]. . . . .	5
2.2	ASCAT swath coverage [2]. . . . .	6
3.1	Plot of all iceberg positions recorded in the consolidated database, which contains data on icebergs over $5 \text{ km}^2$ from 1992 to the present. . . . .	10
3.2	Example enhanced resolution $\sigma^0$ image of iceberg B10a on JD 205, 1999, from QuickScat data. . . . .	12
3.3	Iceberg B15b, on JD 47 of 2005, in QuikSCAT data. This is a scatterometer $\sigma^0$ image in dB. The iceberg appears as a group of lighter pixels in the center of the $660 \times 660 \text{ km}$ image, centered at $64.9 \text{ S}$ , $137.5 \text{ E}$ . . . . .	13
3.4	Iceberg C33 as it calves from the Nansen Ice Shelf, April 7, 2016 [3], as seen in an optical image, courtesy of NASA. . . . .	14
3.5	Example of piecewise cubic interpolation function using the latitude and longitude data provided in the consolidated database. . . . .	16
3.6	Zoomed in plot of the complete track for iceberg B15b. The iceberg leaves the coast of Antarctica at $73.6 \text{ S}$ , $23 \text{ W}$ , near Queen Maud Land. Blue crosses represent interpolated positions for days in which no data is available. . . . .	17
4.1	Original $\sigma^0$ image (top) in $ dB $ compared with the mapped $e_{ij}$ values of iceberg A43c in A from QSCAT data for JD 141 of 2001. The iceberg is in the center of each $660 \times 660 \text{ km}$ image. . . . .	20
4.2	Matrix $P$ for iceberg B15b on JD 297 of 2005 (top), with its corresponding binary image. The iceberg itself has values close to one in $P$ . Other nearby icebergs appear as groups with values less than one. Each image is $660 \times 660 \text{ km}$ in size. . . . .	22
4.3	Plots of estimated areas and SNR values of three different icebergs over 100 day periods. The estimated areas are within 15% of the NIC's noted area for each of the icebergs. Note the drop in SNR from days 334-344 of (e) and the corresponding increase in error of (b). . . . .	25
5.1	Binary images of iceberg B15b on JD 61 (left) and 70 (right) of 2001. Least squares fitted ellipses have been superimposed on the images. Each image is $660 \times 660 \text{ km}$ in size. . . . .	28
5.2	A plot of the error $e_s$ versus the sum of fitted parameters $p$ for simulations done by rotating several iceberg images and elementary shapes. The blue line indicates the fitted line used to bound the predicted rotation error. The fit is chosen so that 90% of the simulated points fall beneath the fitted line. The error $e_s$ has a correlation coefficient of .85 with $p$ . . . . .	32
5.3	A plot of the simulation run to calculate $e_s$ using the binary image of B15b on JD 50 of 2001. The blue line indicates the actual motion of the simulated iceberg, while the red line shows the estimated rotation $\phi$ . The error bars show the predicted bound $e_\theta$ . The mean value of $e_s$ is .0083 radians. . . . .	33

5.4 A plot of rotational estimates for B15b in radians. This is 100 days of QuikSCAT data from JD 47-147 of 2001, with no melt events. The error bars bound the possible angles for a given day. . . . . 33

## CHAPTER 1. INTRODUCTION

Spaceborne wind scatterometers are primarily designed to measure wind speeds over the ocean. Active microwave scatterometers transmit a pulse and measure the returned radar backscatter ( $\sigma^0$ ). This backscatter measurement is then used to measure wind speed, although many other scientific applications have also been developed.

Once such application is the tracking of iceberg movement in the polar regions. Due to surface differences between iceberg, sea ice, and ocean, the  $\sigma^0$  measurement between them are generally different [4]. This difference is leveraged to discriminate between iceberg ice and surrounding water or ice.

The contrast between an iceberg and its surroundings is due mainly to volume scattering from the layers of snow and ice on the surface of tabular icebergs, causing them to appear as contiguous regions of high  $\sigma^0$  regions in scatterometer images. However, during the Austral summer or other times when the surface is undergoing melt, the contrast in  $\sigma^0$  between the iceberg surface and surrounding sea ice can be small due to liquid water at the surface.

Ku-band scatterometers are particularly well suited for iceberg tracking because of the high contrast between  $\sigma^0$  measurements of icebergs compared to the ocean or sea ice. To a lesser extent, lower contrast between  $\sigma^0$  measurements of icebergs and their surroundings from C-band scatterometers can also be used to track their motion.

Scatterometers have a low resolution, with each pixel covering an area of about 25 x 25 km. While other types of sensors, such as optical or infrared, have higher pixel resolution, they are also affected by clouds and seasonal shifts. Microwave scatterometers operate at a much lower frequency, allowing them to penetrate the water vapor contained in clouds and more consistently image the surface of the earth. To enable imaging, and to offset the low resolution of scatterometer data, the Scatterometer Image Reconstruction (SIR) algorithm has been developed in order to enhance scatterometer resolution, allowing for a more detailed  $\sigma^0$  image to be created.

Icebergs were first tracked by satellite microwave remote sensing instruments in 1972 with the launch of the Electrically Scanning Microwave Radiometer (ESMR) [5]. Since then, various scatterometers have been used along with in-situ observations to record iceberg positions and information about their surroundings.

The BYU Microwave Earth Remote Sensing (MERS) Laboratory leverages images created from  $\sigma^0$  measurements to track icebergs and record their daily positions in several databases. Currently, these databases contain information from the Ku-band NASA scatterometer (NSCAT), Quick Scatterometer (QSCAT) [6], and Ocean Scatterometer (OSCAT), and from the C-band Advanced Scatterometer (ASCAT), as well as sporadic positions from earlier spaceborne satellites such as the ERS and SASS. Other agencies, such as the National Ice Center (NIC), record iceberg positions using a variety of other methods, including optical and infrared sensors, and in-situ observations from ships.

NSCAT and QSCAT consistently gathered daily  $\sigma^0$  data for the duration of their respective missions. The OSCAT mission, which started days after QSCAT failed, ended in February 2014. Several scatterometers, including ASCAT, currently operate in C-band. Although C-band data does not discriminate between sea ice and ocean as well as Ku-band data, ASCAT provides polar scatterometer data beyond the completion of OSCAT's mission.

It is desirable to maintain a database of iceberg positions so as to maintain a single track for each iceberg. This allows researchers to follow particular icebergs more easily and not lose them to melt events or other times in which it is difficult to distinguish a single iceberg from a bright patch of sea ice or another nearby iceberg.

Due to differing data formats, it is difficult to compare measurements from the NIC and BYU MERS databases for tracking purposes. As such, it is desirable to consolidate the two databases into a single, cohesive database with one format.

## **1.1 Thesis Statement**

Due to the differing data formats and time periods discussed above, it is desirable to consolidate iceberg positional measurements from the NIC and BYU MERS databases into one database. For this thesis, a database is developed that provides a consistent format and single location to draw iceberg positions and other derivative measurements from. As an extension of the positional data

provided by this database, algorithms are developed to accurately estimate other iceberg qualities, such as surface area, angular velocity, and general shape, from an iceberg's  $\sigma^0$  contour.

## **1.2 Research Contributions**

In this thesis, the development and methodology of a consolidated BYU/NIC Antarctic Iceberg Tracking Database is presented. The database combines data from the original BYU daily iceberg tracking database derived from scatterometers, and the NIC's weekly Antarctic iceberg tracking database derived from mostly optical and infrared sensors. Using this data, interpolation methods and statistical analyses of iceberg locations are discussed.

The consolidated database is used in an algorithm to derive contours and sizes from satellite data and better understand patterns in iceberg formation and behavior. Starting from scatterometer images, the algorithm uses the relatively constant backscatter values across the surface of an iceberg to derive a contour of its shape. Contours are then used to find an angle of rotation between images taken on successive days. This method produces size estimates that are within 10% of the area given by the NIC.

## **1.3 Thesis Outline**

The thesis is outlined as follows: Chapter 2 contains background information. Chapter 3 discusses the methodology behind the consolidated database. Chapter 4 outlines the algorithm used to provide size estimates. In Chapter 5, the algorithm used to provide rotational estimates is shown, with a conclusion and possible future work discussed in Chapter 6.

## CHAPTER 2. BACKGROUND

Some background information is helpful in order to understand the tracking of Antarctic icebergs using microwave scatterometer images. The following sections discuss the details of two active microwave remote sensors used to create images. Scatterometer backscatter measurements and image reconstruction techniques are examined, and background on iceberg tracking is presented.

### 2.1 Active Microwave Remote Sensing

Active microwave remote sensors are so named because they both transmit and receive microwave pulses. A scatterometer is a type of active sensor that measures the radar backscatter of the Earth's surface. Scatterometers were originally designed to measure wind speeds over the ocean; however, it was found that wind scatterometer data also provides useful information in land and ice applications [7].

Early Ku-band instruments, such as NSCAT, were found useful in measuring polar sea ice extent and locating icebergs in the ocean. However, scatterometers have a low resolution, making the development of algorithms to enhance image resolution necessary for many applications. Such reconstruction techniques create high resolution images of the surface from backscatter ( $\sigma^0$ ) measurements [7]. High resolution images are developed by taking advantage of Doppler filters and/or range gating [4].

#### 2.1.1 QuikSCAT

The SeaWinds instrument on the QuikSCAT satellite (referred to as QuikSCAT) is a conically scanning, dual-polarized pencil-beam scatterometer. QuikSCAT was launched in 1999 and was intended as a "quick recovery" mission following the premature end of the NASA Scatterometer (NSCAT) mission. The satellite was placed in an 803 km altitude, sun-synchronous orbit [8].

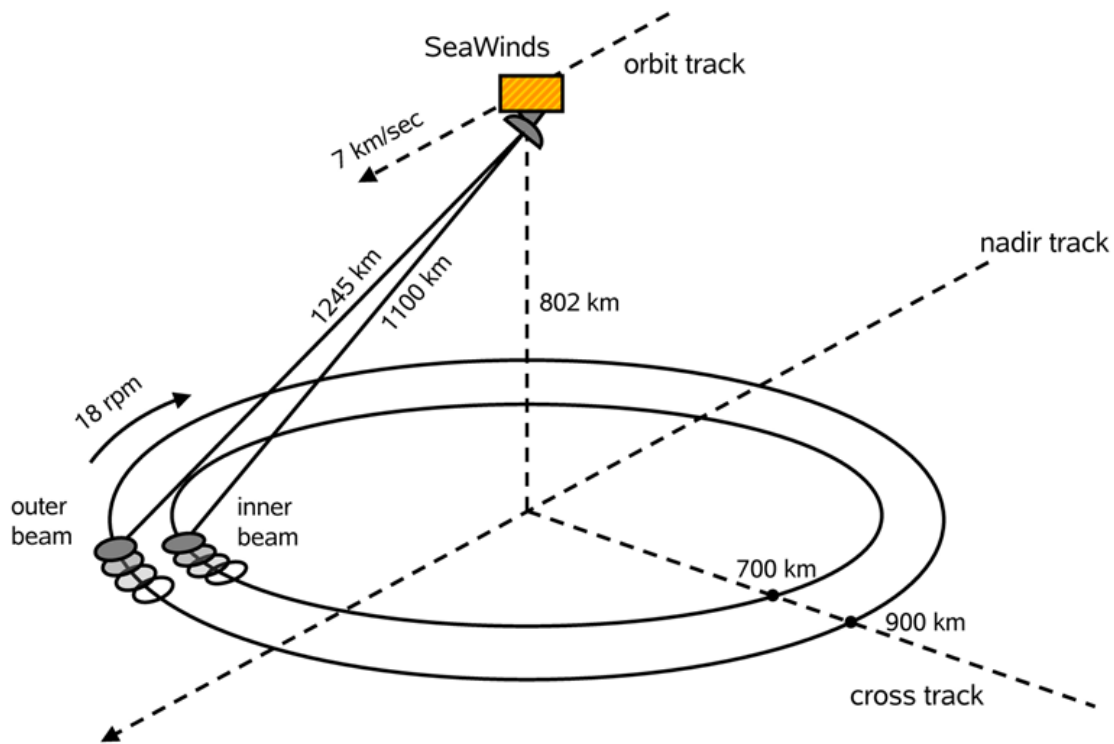


Figure 2.1: QuikSCAT scanning geometry [1].

The mission was intended to only last two years, but continued collecting data until 2009, well past its expected lifetime.

QuikSCAT measures  $\sigma^0$  values on the surface at multiple azimuth angles, which are used to calculate wind vectors. Unlike previous wind scatterometers that had fan-beam geometries, QuikSCAT has a rotating pencil-beam design which allows for multiple azimuth angle measurements at a fixed incidence angle. This scanning geometry is shown in Fig. 2.1. The rotating design improves surface coverage and provides more  $\sigma^0$  measurements in the polar regions, while providing multiple look angles for wind retrieval [9].

### 2.1.2 ASCAT

The first Advanced Scatterometer (ASCAT) was launched by the European Space Agency (ESA) on board the Meteorological Operational (MetOp)-A satellite in October 2006, with data

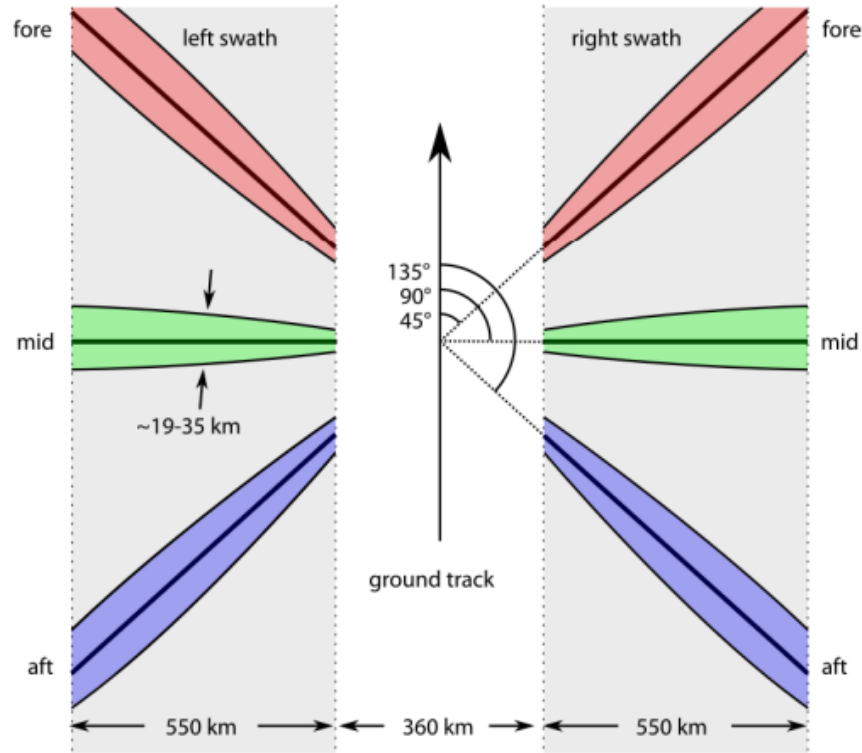


Figure 2.2: ASCAT swath coverage [2].

first collected in May 2007. ASCAT is operated by the European organization for the exploitation of METeorological SATellites (EUMETSAT) [10]. ASCAT is a 5.255 GHz (C-band) fan-beam scatterometer with two sets of three vertically polarized antennas. The three antennas point at 45, 90, and 135 degrees relative to the satellite track. The two sets of antennas are on either side of the instrument. These beams illuminate 550 km-wide swaths on both sides of the flight track with a nadir gap of about 700 km [10]. Because of its limited swath coverage, ASCAT does not achieve full daily polar coverage like QuikSCAT.

## 2.2 Scatterometer Backscatter Measurements

Scatterometers measure the normalized radar backscatter coefficient ( $\sigma^0$ ) of the Earth's surface. The scatterometer transmits pulses to the surface and measures the received backscatter

power  $P_S$ . The  $\sigma^0$  measurement is derived from the radar equation,

$$\sigma^0 = \frac{(4\pi)^3 R^4 L}{P_t G^2 \lambda^2 A} P_S, \quad (2.1)$$

where  $R$  is the slant range to the surface,  $P_t$  is the transmitted power,  $P_S$  is the received backscattered power,  $L$  represents known system losses,  $G$  is antenna gain,  $A$  is the effective illuminated area, and  $\lambda$  is the wavelength of the transmitted radiation [4]. The  $\sigma^0$  measurements are taken over a range of incidence angles. A linear function of the measurement incidence angle

$$10 \log_{10} \sigma^0(\theta) = A + B(\theta - 40^\circ), \quad (2.2)$$

where  $\theta$  is the incidence angle of the observation, models  $\sigma^0$  measurements.  $A$  and  $B$  are functions of the observed surface characteristics.  $A$  is the  $\sigma^0$  value at  $40^\circ$  incidence angle, and  $B$  is the dependence of  $\sigma^0$  on incidence angle.

Scatterometers were not originally designed for imaging; however, by combining multiple passes, high resolution images of  $A$  and  $B$  can be created to support studies of the Earth's surface. The Scatterometer Image Reconstruction with Filter (SIRF) algorithm produces  $A$  and  $B$  images for several scatterometers, including NSCAT and ASCAT [11] [12]. Since the incidence angle of QuikSCAT is essentially constant, only  $A$  images are computed from QuikSCAT data. The SIRF algorithm enhances effective scatterometer image resolution by combining  $\sigma^0$  measurements from multiple passes into a single image. Daily enhanced resolution SIRF images are then used in the iceberg tracking process described below.

### 2.3 Iceberg Tracking Methodology

Icebergs are formed by the calving, or breaking off, of large chunks of ice from glaciers. Glacial ice is freshwater ice formed from compressed layers of snow that have accumulated over many years [13]. Volume scattering due to the layers of ice and snow forming the iceberg cause the surface of the iceberg to appear bright in  $\sigma^0$  images unless the surface is undergoing melt. During melt, the top layers of the iceberg are covered in liquid water, resulting in less contrast between the iceberg and its surroundings.

The contrast in  $\sigma^0$  between an iceberg and its surrounding ocean or sea ice in SIRF A images is used to locate and track the iceberg as it moves [14]. The icebergs discussed in later sections are tabular icebergs, which have flat surfaces and are generally much larger than other types of icebergs. Tabular icebergs greater than  $5 \text{ km}^2$  in area are large enough to be tracked in reconstructed  $\sigma^0$  SIRF images. They may also be tracked by using their backscatter signature, which differs from that of sea ice for sufficiently large icebergs.

Tracking of icebergs using scatterometers has several advantages over optical tracking or infrared imaging. A  $\sigma^0$  image is not affected significantly by the sun, allowing for nighttime imaging. This is particularly desirable in the polar regions, where night may extend for multiple weeks during the austral winter. The frequency bands in which scatterometers operate are also not affected by clouds, allowing for imaging through cloud cover. These advantages largely offset the lower resolution of  $\sigma^0$  images in tracking tabular icebergs over multiple years.

## CHAPTER 3. DATABASE IMPLEMENTATION

### 3.1 Motivation

Databases of current and archived iceberg positions are useful for facilitating many different maritime and scientific pursuits in the Antarctic seas. Marine biologists, for example, seek current iceberg coordinates in order to study iceberg-adjacent ecosystems [15]. Current iceberg positions are used by Antarctic cruise ships, military submarines, and sailor-circumnavigators to facilitate research and business, as well as to avoid collisions. Archived data have been used to study the movement and disintegration of icebergs over time [16], and to validate methods of iceberg detection through hydroacoustic sensing [17] and tracking via altimeter waveform analysis [18].

Two databases are consolidated and enhanced in this thesis; namely, the BYU Microwave Earth Remote Sensing (MERS) Antarctic Iceberg Tracking Database and the National Ice Center (NIC) database. The two databases are currently published in separate locations, each with a unique format. The NIC publishes a collection of coordinate points, iceberg lengths and widths, and some optical photos, using a variety of sources. However, the NIC database is limited to one coordinate per iceberg per week. In contrast, the BYU MERS database has a set of coordinate points for each day that any particular scatterometer is active. This data is separated by sensor (ASCAT, OSCAT, QSCAT, NSCAT, ERS, Seawinds, and SASS) and covers from 1978 to the present day.

Due to differences in the organization of the NIC and BYU datasets, comparing same-day data from the different sources can be difficult. Further, each sensor used by the MERS database has a different mission lifetime, which introduces gaps in the archive over the life of a single iceberg as databases change from one sensor to another. To ameliorate these problems, a consolidated database has been developed to include the features of both databases. The new database is designed to simplify the long-term comparison of archived data.

The information in the new database is organized into two separate sets. Each set is arranged first by iceberg, second by date, with information from all relevant sensors or measurements listed in the same file. At least one original or interpolated position is available for each day of an iceberg's lifetime.

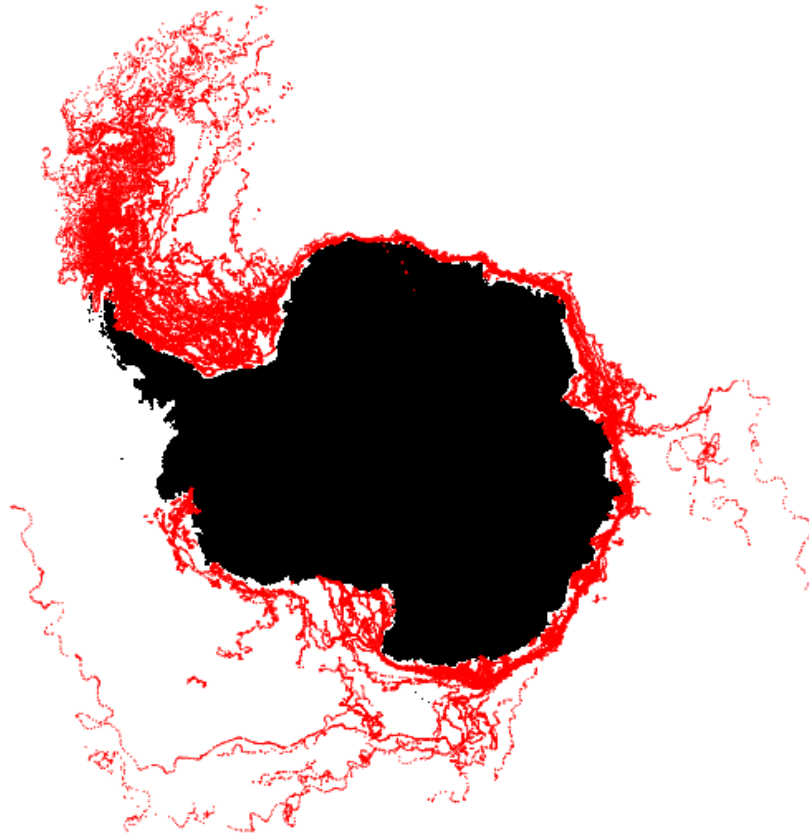


Figure 3.1: Plot of all iceberg positions recorded in the consolidated database, which contains data on icebergs over  $5 \text{ km}^2$  from 1992 to the present.

In this chapter, the methods by which iceberg positions are determined for each database are presented and the method used to create the consolidated database is shown. The process by which the data is interpolated and processed is also examined.

## 3.2 Data Collection

Several different data collection methods are used to both locate and track icebergs in the Antarctic ocean. The positional data generated by these methods is used to create databases of iceberg locations. Two of these databases, along with their data collection methodology, are discussed in this section.

### 3.2.1 BYU MERS Data Collection

Iceberg locations are determined by BYU MERS using daily scatterometer images of the Antarctic region from various satellite scatterometers. MERS first receives scatterometer  $\sigma^0$  measurements, organized by satellite orbit, as L1B or SZF files. Multiple files are combined into a single enhanced resolution  $\sigma^0$  image using the Scatterometer Image Reconstruction (SIR) algorithm [19]. One SIR image is produced for every day of the year for which scatterometer data is available. Iceberg positions are determined by manually identifying the high backscatter regions corresponding to icebergs in these SIR images and correlating them with previously archived positions and the NIC's reported iceberg locations.

The current database published by BYU MERS contains information from seven scatterometers: SASS, ERS, NSCAT, SeaWinds, QuikSCAT, OSCAT, and ASCAT. The earliest data (from SASS) ranges from July to September of 1978. The bulk of the data begins in 1992, with ERS, and continues to the present. MERS position data carries the disclaimer that, because it is collected manually using moderate-resolution satellite  $\sigma^0$  images, its accuracy is limited to plus-or-minus one pixel. Pixel resolution values vary from 2.225 to 8.9 km/pixel according to the sensor used.

The primary backscatter images used in this thesis are Ku-band SIR images created from QuikSCAT data. Since it has been observed that higher frequencies produce more contrast in SIR images, Ku-band is more desirable for iceberg tracking. Contours are also generated using C-band SIR images created from ASCAT data when QuikSCAT data is not available.

Scatterometers, as active sensors that emit radiation, do not rely on solar illumination and are able to perform consistently under nearly all weather conditions. As a general rule, however, scatterometry produces lower-resolution images than optical and I/R sensing. Pixel resolution

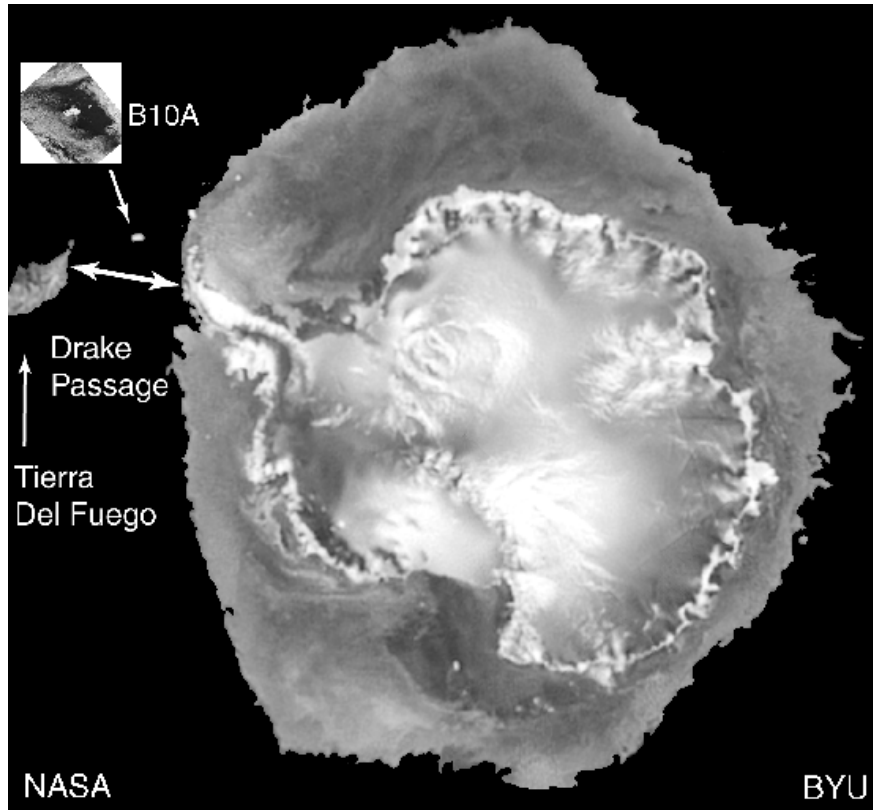


Figure 3.2: Example enhanced resolution  $\sigma^0$  image of iceberg B10a on JD 205, 1999, from QuickScat data.

varies according to the scatterometer used to create the image; a typical QuikSCAT image of Antarctica is  $3880 \times 3880$  pixels, with each pixel covering an area between  $3.42$  and  $5.27 \text{ km}^2$ .

### 3.2.2 NIC Data Collection

The National Ice Center (NIC) is a United States governmental organization comprised of three individual agencies: the United States Navy, the National Oceanic and Atmospheric Association (NOAA), and the United States Coast Guard. Although the establishment of the NIC was not official until 1995, data collected by the Joint Ice Center (a collaboration between NOAA and the Navy [prior to the addition of the Coast Guard]) dates back to 1976 and is included in the NIC database.

About once per week, the NIC publishes the current latitude and longitudinal positions of most icebergs within a specified area and above a specified size. It also publishes each iceberg's

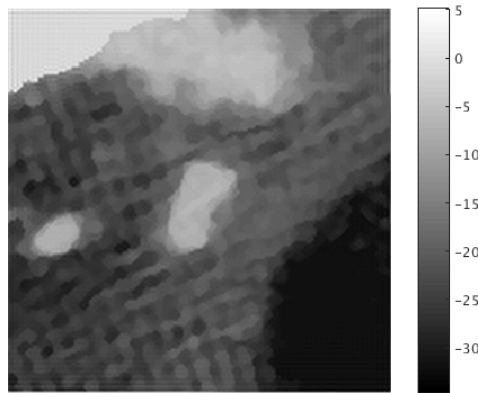


Figure 3.3: Iceberg B15b, on JD 47 of 2005, in QuikSCAT data. This is a scatterometer  $\sigma^0$  image in dB. The iceberg appears as a group of lighter pixels in the center of the  $660 \times 660$  km image, centered at  $64.9$  S,  $137.5$  E.

length and width, measured in nautical miles. The current data can be accessed at the NIC website. Archived data is available from them on request.

The NIC determines iceberg coordinates primarily from images from spaceborne sensors, including the Environmental Satellite (EnviSat), Advanced Very High Resolution Radiometer (AVHRR), Moderate Resolution Imaging Spectroradiometer (MODIS), and Radarsat. A portion of the data comes from ship reports. Other contributions stem from the Defense Meteorological Satellite Program (DMSP) and Argos. The majority of sensors utilized by the NIC are passive optical or infrared (I/R) sensors.

Images collected by optical and I/R sensors are typically intuitive and relatively easy to interpret. However, optical sensors depend on visible light from the sun; when sunlight is absorbed by clouds, or limited by changing seasonal patterns, optical sensors do not function at peak performance or produce useful images. I/R sensors are likewise affected by clouds and seasonal shifts [20]. This is particularly consequential in polar regions such as Antarctica, where the sun does not rise for multiple weeks during the winter and clouds are common.

### 3.3 Data Interpolation and Processing

Before 1999, daily scatterometer measurements of the Antarctic region were not possible due to the particularities of the satellites in orbit at the time. In order to maintain a consistent time

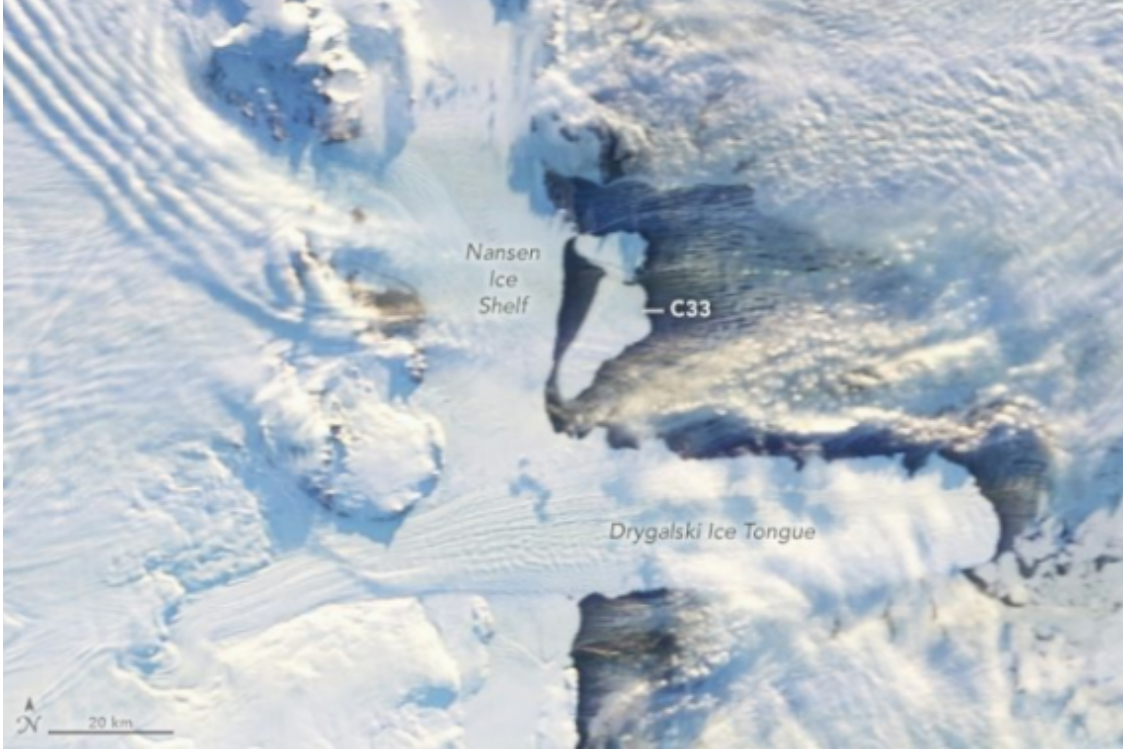


Figure 3.4: Iceberg C33 as it calves from the Nansen Ice Shelf, April 7, 2016 [3], as seen in an optical image, courtesy of NASA.

period between measurements in the consolidated database, some estimation of iceberg positions is necessary over short date gaps.

Iceberg positions for days without a measurement are estimated with a piecewise cubic interpolation between consecutive reported measurements [21]. The interpolation is done by partitioning the latitude or longitude values of the whole iceberg track into  $i = 1, 2, \dots, n$  subintervals  $I_i = [x_i, x_{i+1}]$ , then constructing a monotone piecewise cubic function  $p(x)$  on each subinterval such that

$$p(x_i) = f_i, \tag{3.1}$$

where  $f_i$  is a set of monotone data values at each of the partition points.

In each interval,  $p(x)$  is a cubic polynomial represented as

$$p(x) = f_i H_1(x) + f_{i+1} H_2(x) + d_i H_3(x) + d_{i+1} H_4(x), \tag{3.2}$$

where  $d_i$  is the derivative of  $p(x_i)$  and  $H_k(x)$  are cubic Hermite basis function for the interval  $I_i$ :

$$\begin{aligned}
H_1(x) &= \phi \left( \frac{(x_{i+1} - x)}{h_i} \right), \\
H_2(x) &= \phi \left( \frac{x - x_i}{h_i} \right), \\
H_3(x) &= -h_i \psi \left( \frac{x_{i+1} - x}{h_i} \right), \\
H_4(x) &= h_i \psi \left( \frac{x - x_i}{h_i} \right), \\
\phi(t) &= 3t^2 - 2t^3, \\
\psi(t) &= t^3 - t^2, \\
h_i &= x_{i+1} - x_i.
\end{aligned} \tag{3.3}$$

Using this method produces a  $p(x)$  with the same latitude or longitude values as those found in the interval  $I_i$ , and whose derivative  $p'(x)$  agrees with the derivative of the latitude and longitude values as well. Interpolation is done over the entire set of latitude or longitude points to create a continuous, slowly varying function with no fast oscillations, which is consistent with observed iceberg motion in the polar seas.

Latitude and longitude values are interpolated separately. An example of the separate interpolations is shown in Fig. 3.5. To maintain accuracy, I have chosen not to interpolate iceberg positions between measurements gathered more than two weeks apart. Interpolated position data is provided alongside the original data in the compiled database.

In order for the interpolation to be as accurate as possible, an aggregate of all available recorded sensor measurements for a given track is used to determine the curve of best fit between the two endpoints of any data gaps in the track. Any sensor measurements that fall on the same day are averaged together to produce a single position for that day. The averaged positions are used in the interpolation process to ensure that the final interpolated track is as close to all reported sensor positions as possible, reducing the error of the interpolated daily positions.

The location of an iceberg on any day of its lifetime is given using this track. With the assumption that the center of the iceberg lies close to the reported position in the database, estimates of its size and other derivative measurements are determined.

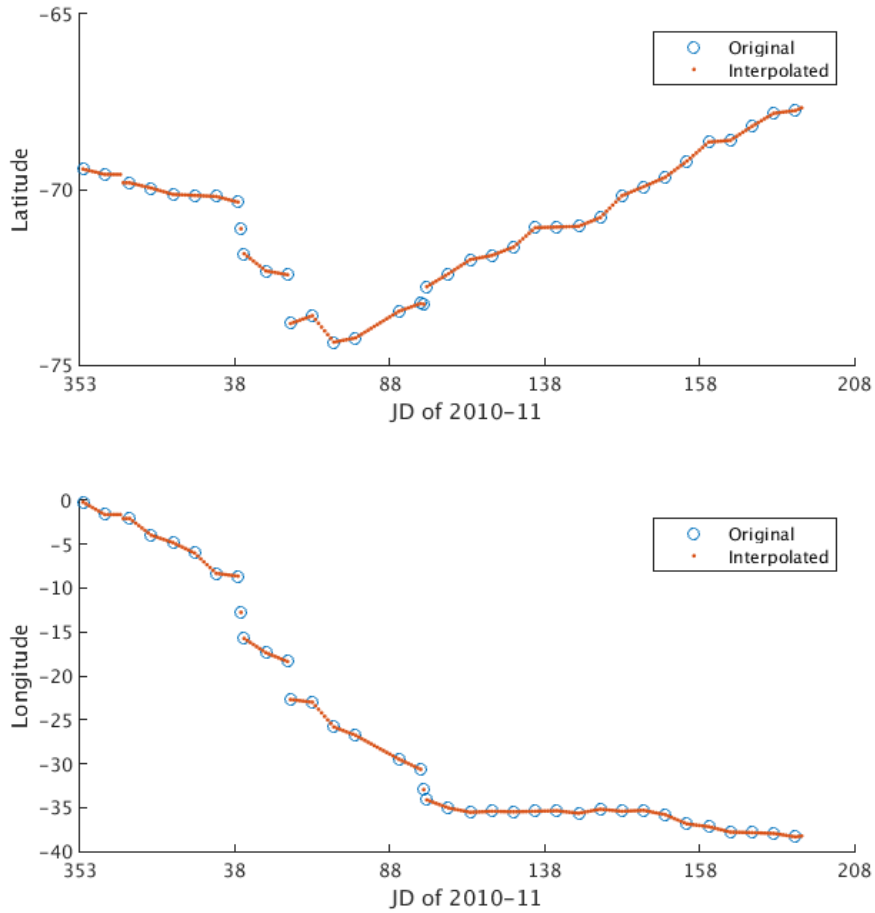


Figure 3.5: Example of piecewise cubic interpolation function using the latitude and longitude data provided in the consolidated database.

### 3.4 Summary

In this chapter, the source data and consolidation of a new iceberg position database is discussed. The database contains information for 553 Antarctic tabular icebergs, with the first positions reported by the SASS scatterometer in 1978, and continuing to the present with data recieved by currently operating scatterometers, such as ASCAT. Positions are given by manually selecting the center of an iceberg in an optical or backscatter image, and as such are considered to be accurate to plus or minus a few pixels (between 7 and 15 *km* depending on the resolution of the sensor used). A more detailed description of the format of the new database is given in Appendix A.

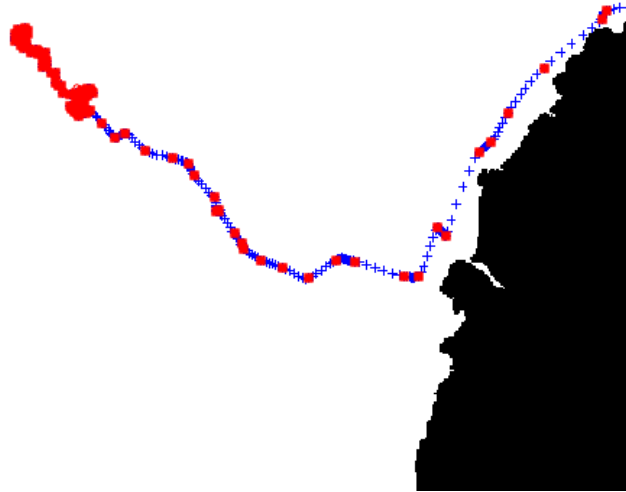


Figure 3.6: Zoomed in plot of the complete track for iceberg B15b. The iceberg leaves the coast of Antarctica at 73.6 S, 23 W, near Queen Maud Land. Blue crosses represent interpolated positions for days in which no data is available.

While the database is mostly complete from 1992-2017, there are gaps in the positional record for days in which no sensors were active. In order to model iceberg tracks during such gaps, a piecewise cubic interpolation algorithm is used to fill in these gaps. With the interpolated points, the new database has complete tracks for nearly all included icebergs. The location of an iceberg on any day of its lifetime is given using this track. With the assumption that the center of the iceberg lies close to the reported position in the database, estimates of its size and other derivative measurements are determined.

## CHAPTER 4. SIZE ESTIMATES

### 4.1 Introduction

Archived iceberg positional data can be used for more derivative measurements as well. Estimating the geometrical size and shape of tabular Antarctic icebergs from images is desirable to help better understand patterns in iceberg formation and behavior. By using the recorded position for an iceberg, along with these images, a contour of an iceberg's size and shape can be generated.

Rough iceberg sizes are currently published weekly by the National Ice Center (NIC). However, these size estimates are generated manually. This is undesirable due to the effort and manpower required for training and accuracy. With a computer generated contour of an iceberg, the area of its surface can be determined, providing an easy and consistent means of obtaining daily size estimates of icebergs on any day where satellite data has been collected.

To estimate the size of an iceberg, I first find a contour of its surface in the  $\sigma^0$  image. An iceberg's contour is a closed curve that completely encompasses the iceberg as seen from above; i.e., from a satellite's perspective. Estimating the size of an iceberg from its contour requires fitting the contour as closely as possible to the iceberg while removing any image pixels that do not belong to the iceberg. This involves distinguishing the iceberg's  $\sigma^0$  values from surrounding sea ice and ocean water.

Over the entire polar region, many different areas have  $\sigma^0$  values similar to the iceberg. In order to isolate an individual iceberg, I focus on an area around the iceberg, centered on its archived position. From that area, a mapping function creates a feature vector that is used to identify the pixels belonging to the iceberg of interest. A contour is then drawn around the iceberg pixels and used to compute the area of the iceberg itself, with some filtering done on the end results to improve accuracy and reduce noise. This procedure is described in detail in the following subsections.

## 4.2 Windowing

In order to isolate an individual iceberg from the rest of the polar region, a windowed area is first selected around the iceberg. A windowed area can be any size; I have empirically determined that a  $150 \times 150$  pixel area is sufficient to effectively distinguish an iceberg from its surroundings while being large enough to cover the largest icebergs and minimize computation time. This allows us to represent the local backscatter image as a  $150 \times 150$  matrix  $A$ .

The same windowing process is also completed for a separate matrix  $V$ , composed of the variance of each pixel in  $A$  calculated from the difference between the forward projection of  $\sigma^0$  in the image and the measurements used to create the image. The  $V$  matrix values serve to help distinguish between iceberg ice and surrounding ocean. The latter exhibits rapid changes in  $\sigma^0$  values and consequently has higher variance. The iceberg can thus be identified in  $V$  by finding pixels with smaller variance values. Both the  $A$  and  $V$  matrices are used in the mapping process described below to distinguish iceberg from other features in the SIR backscatter images.

## 4.3 Mapping

A value mapping function helps to discriminate between the iceberg  $\sigma^0$  values and other features inside the window. To find the pixels inside of the contour, all elements  $e$  in  $A$  and  $V$  are mapped according to

$$e_{ij} = |e^* - e_{ij}|^2,$$

where  $e^*$  is the value of  $\sigma^0$  or the calculated variance at the archived position of the iceberg.

Mapping in this way increases the numerical distance between the iceberg  $e$  values and other values I do not want to include in the contour estimate, while also placing the archived  $e$  values of the iceberg at the origin of the transformed coordinate system. By extracting from each pixel a feature vector composed of its value in the matrices  $A$  and  $V$ , I am able to calculate both the Euclidean and Mahalanobis distances of the pixel feature vector value from the origin. Since there is generally little variation in  $\sigma^0$  over the iceberg's surface, I assume that the  $\sigma^0$  and variance values of the iceberg are found within a certain threshold.

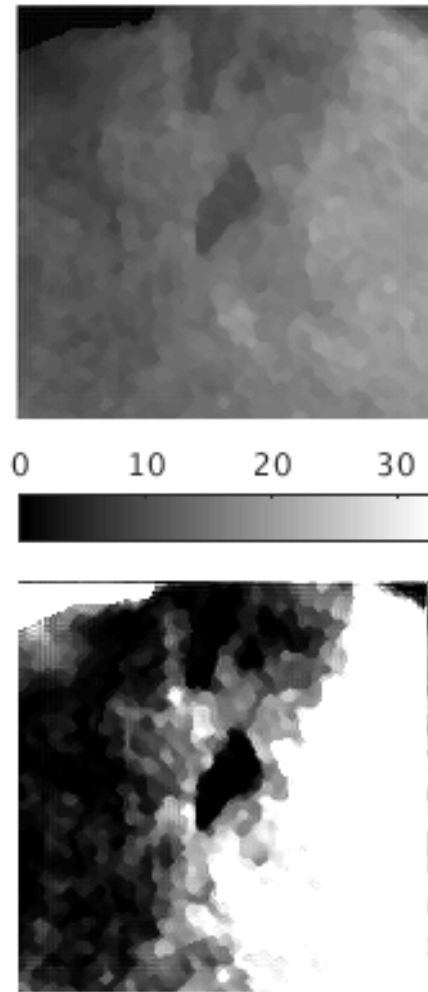


Figure 4.1: Original  $\sigma^0$  image (top) in  $|dB|$  compared with the mapped  $e_{ij}$  values of iceberg A43c in  $A$  from QSCAT data for JD 141 of 2001. The iceberg is in the center of each  $660 \times 660$  km image.

#### 4.4 Adaptive Threshold

In order to determine which of the pixels in  $A$  and  $V$  belong to the iceberg, iceberg pixels are separated from the background image. This is done using an adaptive threshold determined by variational minimax optimization [22]. In variational minimax optimization, the optimization is done on an energy functional formed by an edge sensitive data term and a regularization term. The

energy functional is defined as

$$E(T, \alpha) = \sqrt{1 - \alpha^2} E_1(T) + \alpha E_2(T), \quad (4.1)$$

where

$$\begin{aligned} E_1(T) &= \frac{1}{2} \iint h(x,y) (I(x,y) - T(x,y))^2 dx dy, \\ E_2(T) &= \frac{1}{2} \iint |\nabla T(x,y)|^2 dx dy, \\ h(x,y) &= \frac{|\nabla I(x,y)|^2}{\max(|\nabla I(x,y)|^2)}, \end{aligned} \quad (4.2)$$

$I$  is the image function,  $T$  the threshold function, and  $\alpha$  is a weighting parameter given by finding the minimum of  $E$ , differentiating with respect to  $\alpha$ .

Once  $\alpha$  has been found, the optimal threshold function  $T$  is found by solving the differential equation

$$\frac{\partial T}{\partial t}(x,y) = \sqrt{1 - \alpha^2} (h(x,y) (I(x,y) - T(x,y)) + \alpha (\nabla^2 T(x,y))) \quad (4.3)$$

using a gradient descent technique. All pixels in  $I$  with values greater than the corresponding pixel in  $T$  are flagged to make a binary image, which is then used to create a contour of the iceberg.

#### 4.5 Contour Estimation

The iceberg is contoured in an iterative process using the Euclidean and Mahalanobis distance metrics. The process begins by creating a matrix  $P$  from the inverse Euclidean distance values of all pixels in the windowed area. In this way, pixel values farther from the origin - the location of the archived iceberg pixel values - are weighted less heavily in  $P$ , the elements of which are considered to be the likelihood of a pixel belonging to the iceberg.

A binary image is created from  $P$  using the adaptive thresholding algorithm discussed in the previous section. Once this binary image is created, erosion and dilation are applied to remove any outlying flagged pixels. The remaining flagged pixels are used to create a covariance matrix  $R$ , from which the Mahalanobis distance of each pixel in the windowed area is calculated [23]. Mahalanobis distance is a measure of the number of standard deviations from a point to the mean of

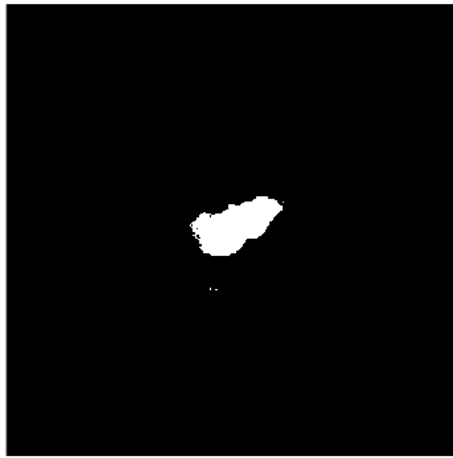
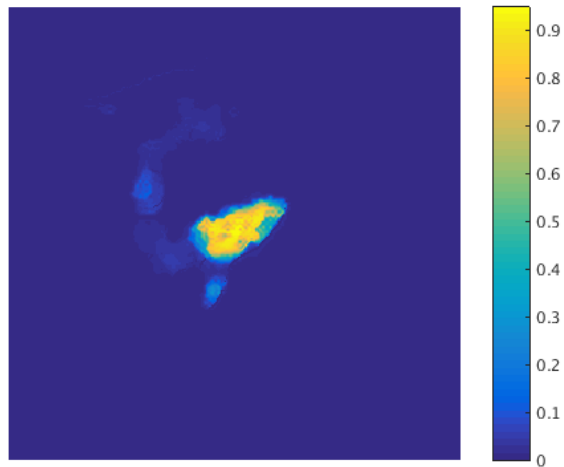


Figure 4.2: Matrix  $P$  for iceberg B15b on JD 297 of 2005 (top), with its corresponding binary image. The iceberg itself has values close to one in  $P$ . Other nearby icebergs appear as groups with values less than one. Each image is  $660 \times 660 \text{ km}$  in size.

a distribution  $D$ . In this case,  $D$  is a Gaussian distribution centered at the origin with covariance of  $R$ . The inverse distance values are added to  $P$ , where calculation of the threshold function, erosion, and dilation are applied as before to create the final binary image of iceberg pixels. Examples of  $P$  and the final binary image are given in Fig. 4.2.

The MATLAB “boundary” command is then used on the final binary image to draw a contour around the iceberg pixels. The iceberg area is computed with the aid of an array of pixel sizes, with the area value of each pixel inside the contour being added together to produce a size estimate

in  $km^2$ . While this method removes most of the incorrectly selected pixels near the iceberg, it fails to account for larger groups of pixels belonging to other icebergs near the sides of the windowed area. These pixels are removed using an apodization window.

#### 4.5.1 Apodization Window

The iceberg is placed in the center of the windowed area during the creation of  $A$  and  $V$ . Any pixels far from the window center are assumed to not be part of the iceberg and are weighted in  $P$  by an apodization window, given as

$$p_{ij} = y(i)y(j), \quad (4.4)$$

where

$$y(x) = \begin{cases} \frac{1}{2}1 + \cos(\frac{2\pi}{r}[x - \frac{r}{2}]), & 0 \leq x < \frac{r}{2} \\ 1, & \frac{r}{2} \leq x < 1 - \frac{r}{2} \\ \frac{1}{2}\{1 + \cos(\frac{2\pi}{r}[x - 1 + \frac{r}{2}])\}, & 1 - \frac{r}{2} \leq x \leq 1 \end{cases} \quad (4.5)$$

is a tapered cosine window filter with a stretching coefficient  $r$ , determined as a ratio of the estimated contour's area to the window area, to adjust for iceberg size.

To avoid adding single points to the contour that fall outside of the iceberg's shape,  $P$  is convolved with a discrete approximation of a two dimensional isotropic Gaussian using the equation

$$q_{ij} = \sum_{k_1=-\infty}^{\infty} \sum_{k_2=-\infty}^{\infty} p_{ij}f(i - k_1, j - k_2), \quad (4.6)$$

where

$$f(x, y) = \frac{1}{2\pi\sigma^2} e^{-\frac{x^2+y^2}{2\sigma^2}} \quad (4.7)$$

is sampled at integer values of  $x$  and  $y$ . The standard deviation  $\sigma$  was chosen empirically to be one.

This convolution averages out areas with higher spatial frequency in  $P$ . By removing higher frequency components, any superfluous local maxima are removed and a smoother surface is achieved, which enables more accurate calculation of the threshold function. This process

also averages out any single points of higher value in  $P$ , setting them below the threshold and consequently removing them from the final iceberg contour.

#### **4.5.2 Noise Filtering**

Many different sources of noise affect size estimation using microwave images. Changes in temperature near an iceberg, for example, can affect the surrounding region's  $\sigma^0$  values due to melting or freezing sea ice. The quantization introduced by pixels in an image also discretizes the range of possible size estimates from that image. These are removed by filtering the size estimates generated over time.

Noise sources are jointly accounted for by flagging all pixels in  $P$  within  $\pm 5\%$  of the threshold function and setting these as the upper and lower bounds of possible sizes for the windowed iceberg on the given day. Size error is taken to be the difference between these bounds and the filtered size estimate for that day.

An iceberg typically only varies slowly in size, with the exception of calving events. As such, any rapid changes in the size estimates of the iceberg are considered to be noise and are filtered out in a multistep process. First, Hampel identification removes any outliers by replacing them with a weighted average of the surrounding estimates. The weights are given by a signal to noise ratio defined in the next section. Then, a Savitzky-Golay first order filter [24] is applied to the estimates. The filtered output is on average closer to the NIC's published sizes than the original unfiltered output.

#### **4.6 Verification**

In order to verify the reliability of the estimates generated using this algorithm, I use a form of signal to noise ratio (SNR). SNR is found by taking the mean value of all pixels in  $P$  within the iceberg contour and dividing by the mean of all pixels in  $P$  that do not fall within the contour. This measure of SNR is inversely correlated with the difference between generated size estimates and the NIC's published sizes; that is, high SNR tends to indicate agreement with the NIC sizes.

The estimates were compared to NIC sizes over 100 day periods during the lifetime of several icebergs included in the database. An example of several of these periods is given in Fig. 4.3. After removing estimates with low SNR, the average difference from the NIC sizes is 9.7%.

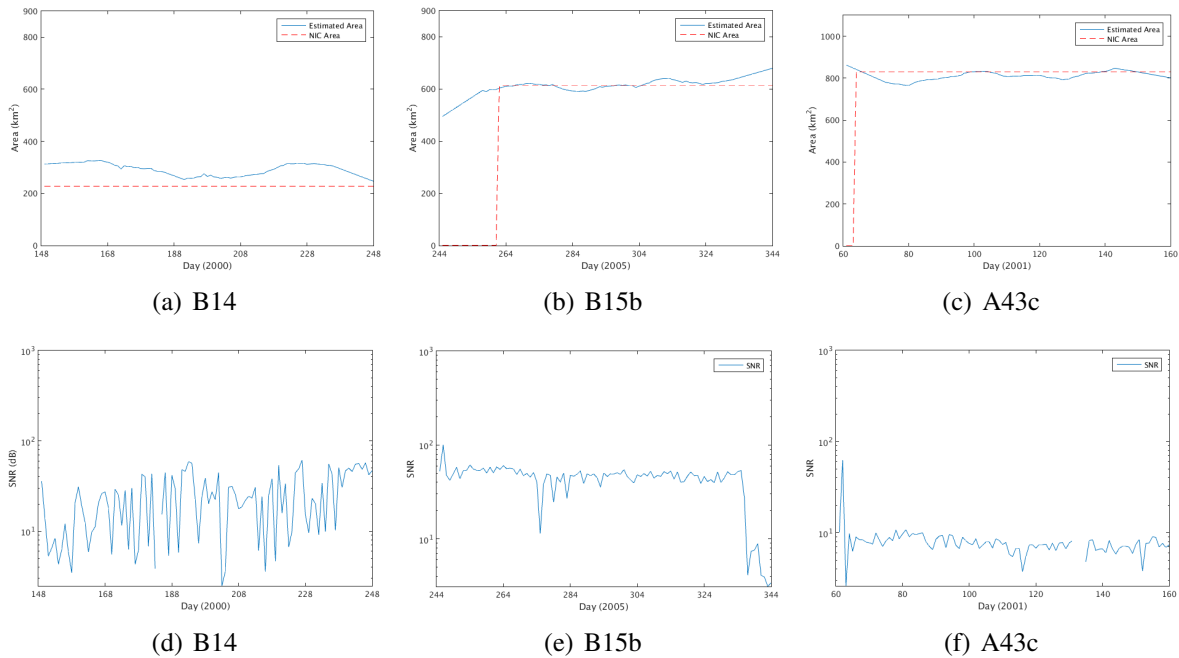


Figure 4.3: Plots of estimated areas and SNR values of three different icebergs over 100 day periods. The estimated areas are within 15% of the NIC’s noted area for each of the icebergs. Note the drop in SNR from days 334-344 of (e) and the corresponding increase in error of (b).

## 4.7 Summary

Starting with the positions provided by the consolidated iceberg database discussed in the previous chapter, an algorithm for estimating the size of an iceberg on any day of its lifetime is developed. This algorithm uses the reported positions along with SIR  $\sigma^0$  images to select pixels belonging to an individual iceberg, then applies a grid of pixel sizes to determine the size in  $km^2$  of the iceberg.

While this algorithm is accurate for most days of iceberg’s lifetime, it does not provide accurate estimates during melt events. Melt events reduce the  $\sigma^0$  contrast between an iceberg and surrounding sea ice, land, or ocean water, making it difficult or impossible to discriminate

between them. Also, some icebergs, such as C19a, are large enough that only a part of the iceberg undergoes a melt event at one time. Such partial melt events also reduce the accuracy of size estimates; however, this is mitigated by filtering the estimates over time.

One way of determining the accuracy of a size estimate is the SNR of an iceberg to its surroundings; low SNR generally indicates a less accurate estimate. Estimates are also compared to the NIC's reported sizes as another measure of accuracy. High SNR estimates generated using this algorithm have an average difference of less than 10% from the NIC sizes. With accurate size estimates, other quantities such as rotational motion of icebergs can be measured.

## CHAPTER 5. ROTATION ESTIMATES

### 5.1 Introduction

One of the measurements that can be derived from iceberg contours is the rotational motion of the iceberg. Estimating the rotational motion of Antarctic icebergs is desirable for building models of ocean currents, which can be difficult to model by other means. Accurate estimates of iceberg rotational motion are also useful in creating models of iceberg translational motion, which allow for prediction of iceberg positions in the future. Information of this kind is useful to many different disciplines and can be helpful in guiding decision making for economic and scientific endeavors, such as the production of fresh water for human consumption or the safety of ocean-based oil rigs [25].

One method of estimating the rotational speed and direction of Antarctic tabular icebergs is presented in this chapter, building on the size estimation algorithm developed in the previous chapter. By fitting an ellipse to the contour generated by the size estimation algorithm and comparing it to the previous day's generated contour, rotational estimates are generated. This process is discussed in detail in the following sections.

### 5.2 Ellipse Fitting

Once an accurate contour is obtained as described in the previous chapter, rotational estimates are calculated. To do this, the generated contour for a particular day is compared to the previous day by fitting an ellipse to the contour using a least squares approximation [26].

The canonical equation for a two dimensional ellipse is

$$Ax^2 + Bxy + Cy^2 + Dx + Ey + F = 0. \quad (5.1)$$



Figure 5.1: Binary images of iceberg B15b on JD 61 (left) and 70 (right) of 2001. Least squares fitted ellipses have been superimposed on the images. Each image is  $660 \times 660$  km in size.

This is represented as a second order polynomial

$$\begin{aligned}
 P(\mathbf{a}, \mathbf{x}) &= \mathbf{a}\mathbf{x} = Ax^2 + Bxy + Cy^2 + Dx + Ey + F = 0, \\
 \mathbf{a} &= \begin{bmatrix} A & B & C & D & E & F \end{bmatrix}, \\
 \mathbf{x} &= \begin{bmatrix} x^2 & xy & y^2 & x & y & 1 \end{bmatrix}^T
 \end{aligned} \tag{5.2}$$

and  $F(\mathbf{a}; \mathbf{x}_i)$  is defined to be the distance of a point  $(x, y)$  to the conic  $P(\mathbf{a}; \mathbf{x}) = 0$ .

With a defined distance metric, I fit a conic to the contour by minimizing the sum of squared distances

$$D(\mathbf{a}) = \sum_{i=1}^N F(\mathbf{x}_i)^2 \tag{5.3}$$

of the curve to the  $N$  data points  $\mathbf{x}_i$ . The solution is forced to be an ellipse by constraining the system's discriminant  $B^2 - 4AC$  to be negative. In solving for the vector  $\mathbf{a}$ , I find the constants needed for the two dimensional ellipse that best fits the iceberg contour in a least squares sense. Examples of these ellipses and how they fit a given contour are shown in Figure 5.1. The constants are used to find an angle of rotation for the iceberg via eigenvalue decomposition as shown in the next section.

### 5.3 Angle Estimation

In order to extract an angle measurement from the least squares fitted ellipse, I find the rotation matrix that corresponds to the ellipse defined by Equation 5.1. This equation, in matrix

form, is

$$[x, y] \begin{bmatrix} A & \frac{B}{2} \\ \frac{B}{2} & C \end{bmatrix} \begin{bmatrix} x \\ y \end{bmatrix} + [D, E] \begin{bmatrix} x \\ y \end{bmatrix} + F = 0. \quad (5.4)$$

Eigenvalue decomposition of the first terms is used to find the rotation matrix  $R$  as

$$\begin{bmatrix} A & \frac{B}{2} \\ \frac{B}{2} & C \end{bmatrix} = R \begin{bmatrix} \lambda_1 & 0 \\ 0 & \lambda_2 \end{bmatrix} R^{-1}, \quad (5.5)$$

where

$$R = \begin{bmatrix} c & -s \\ s & c \end{bmatrix}. \quad (5.6)$$

The second and third terms of the ellipse equation describe the location of the ellipse in space and are not considered in the angle calculation.

The final angle estimate for the ellipse is

$$\phi = \tan^{-1} \frac{c}{s} \quad (5.7)$$

using the first eigenvector of the rotation matrix, which corresponds to the major axis of the ellipse. As  $\phi$  is considered to be the total angle of an iceberg from north as a function of time, the daily rotation estimate is found as

$$\theta = \frac{d\phi}{dt},$$

differentiating over the period of one day. The resulting curve is then smoothed using the Savitsky-Golay filter, with the difference between the filtered and unfiltered curves denoted by  $f_s$ .

This method does not account for single-day rotations of greater than 180 degrees. Also, the contrast between an iceberg and its surroundings can distort the contour shape. As the rotational estimate is susceptible to changes in the iceberg's shape, I account for this in the error calculation as given below.

### 5.3.1 Error Bounds

Several factors are taken into account in order to estimate the error bounds of the rotation estimates, including the difference between contours, the R-square value of the fitted ellipse, the ellipticity of the least squares fitted ellipse of each contour, and the derivative of the rotation estimate. These factors are defined below.

A turning function  $\phi(s)$  is used to quantify the difference between two contours.  $\phi(s)$  measures the change of angle  $\phi$  along a given curve as a function of the normalized curve length  $s$ . Since  $\phi(s)$  is angle and translation independent, the difference between two contours can be taken as the L2 norm of the difference between their turning functions [27], given as

$$\varepsilon = \left[ \int_0^1 (\phi_1(s) - \phi_2(s+u) + \alpha)^2 ds \right]^{\frac{1}{2}}, \quad (5.8)$$

where

$$\alpha = \int_0^1 [\phi_1(s) - \phi_2(s)] ds - 2\pi u. \quad (5.9)$$

The parameter  $u$  is the starting point of the turning function on the contour. It is chosen by filtering and sampling each contour at the same points on  $\phi_1(s)$  and  $\phi_2(s)$ , and taking as  $u$  the sampled point where the L1 norm between the two contours is the smallest.

Error is also introduced in the estimate by the interpolation used to find points for the least squares fitting algorithm. One measure of the goodness of fit of the ellipse to a given set of data points is the R-square ( $R_s$ ) of the fit. R-square is defined as the ratio of the sum of squares of the regression

$$SSR = \sum_{i=1}^n w_i (\hat{y}_i - \mu_y)^2 \quad (5.10)$$

and the total sum of squares

$$SST = \sum_{i=1}^n w_i (y_i - \mu_y)^2, \quad (5.11)$$

giving

$$R_s = \frac{SSR}{SST}. \quad (5.12)$$

$R_s$  is a measure of how successful the fit is in explaining the variation of the data, and can take on any value between 0 and 1. A value close to 1 means that the fit accounts for a greater proportion of the variance in the data.

The ellipticity of an iceberg contour also has bearing on the bounds of rotational error. Since I am fitting an ellipse to the generated contour, the difference between the major and minor axes of the fitted ellipse are correlated with the ability to detect rotational motion. This difference is quantified by using the eigenvalues of Equation 5.5 to represent the length of the ellipse axes. The difference metric is given by

$$\lambda_d = |\lambda_1| - |\lambda_2|, \quad (5.13)$$

where  $\lambda_1$  and  $\lambda_2$  are the maximum and minimum eigenvalues of the ellipse.

In order to set bounds on the rotational error, simulations are run on binary images of various iceberg contours. Binary images of a circle, along with several rectangles of different  $\lambda_d$  values, are also included. Monte Carlo gaussian noise with zero mean and  $\sigma^2$  ranging from .01 to .9 is added to the binary images before the contour process to simulate noisy iceberg contours. By rotating these images over all possible angles and finding the difference  $e_s$  between the calculated rotational estimate and the modeled rotation, I empirically fit an error function to the parameters that show correlation with  $e_s$ . This error function is found to be

$$\begin{aligned} e_\theta(p) &= .9323(p) + .2763, \\ p &= .06f_s + .69|\theta| - .18\lambda_d - .004\varepsilon - .04R_s, \end{aligned} \quad (5.14)$$

where  $f_s$  is the difference between the filtered and unfiltered rotation estimates,  $\theta$  is the derivative of  $\phi$  as shown in Equation 5.7,  $\lambda_d$  is the difference between eigenvalues,  $\varepsilon$  is the shape error, and  $R_s$  is the R-square of the ellipse. A plot of  $e_\theta$  versus the sum of fitted parameters  $p$  is shown in Figure 5.2.

## 5.4 Summary

Starting with iceberg contours generated using the size algorithm discussed in the previous chapter, an algorithm for determining the rotational motion of an iceberg is developed. This algorithm uses an ellipse fitted to the iceberg contour to determine the angle of the iceberg's major axis

with true north, then compares the angle to the previous day to determine the rotational velocity of the iceberg.

Using simulated iceberg contours, I have found that the rotational velocity estimates generated with this algorithm are on average accurate to .01 radians/day. A plot of one simulation is shown in Fig. 5.3. However, during melt events or for days with no reported positions, rotational estimates cannot be accurately generated. The contrast between an iceberg and its surroundings influences the accuracy of rotational estimates, as does the fit of the ellipse to the iceberg contour. As a rule, however, accurate size estimates produce accurate rotation estimates as well.

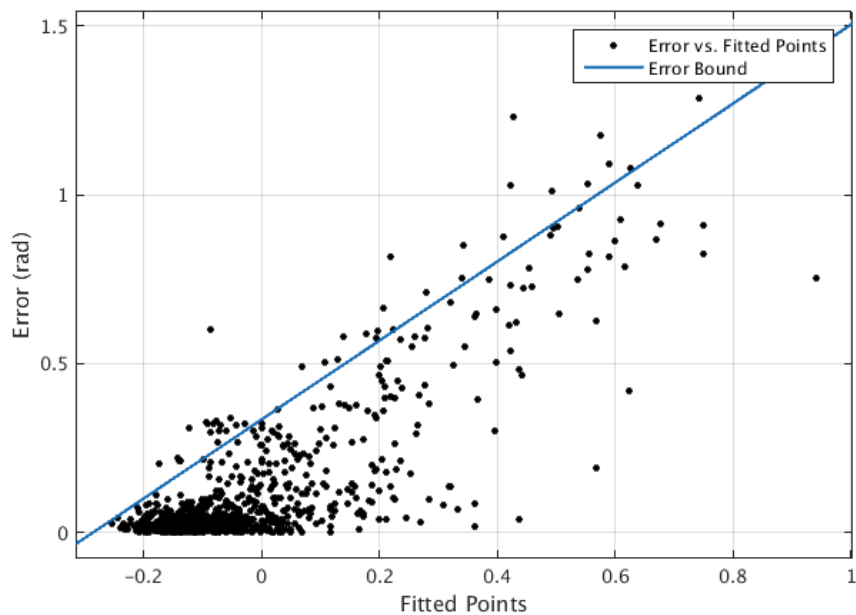


Figure 5.2: A plot of the error  $e_s$  versus the sum of fitted parameters  $p$  for simulations done by rotating several iceberg images and elementary shapes. The blue line indicates the fitted line used to bound the predicted rotation error. The fit is chosen so that 90% of the simulated points fall beneath the fitted line. The error  $e_s$  has a correlation coefficient of .85 with  $p$ .

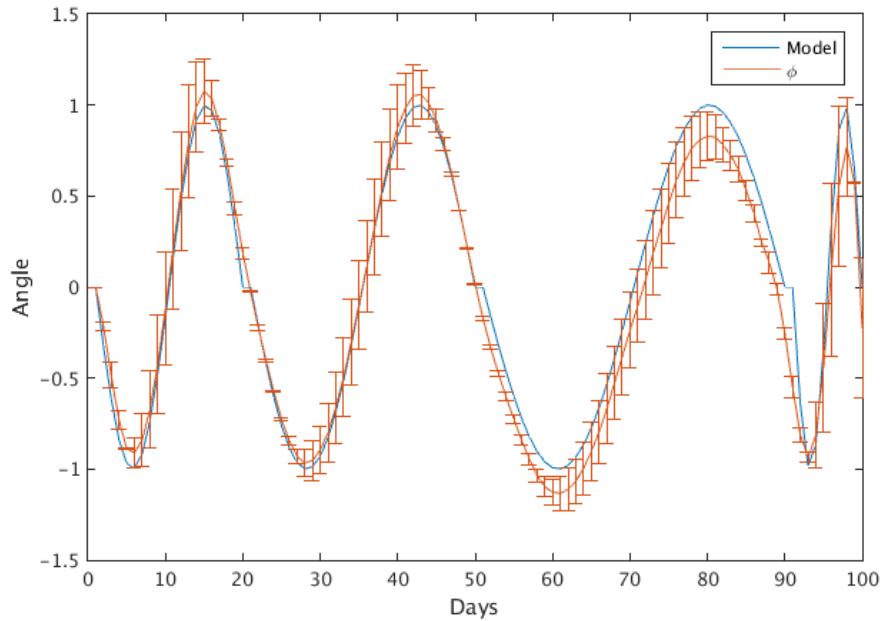


Figure 5.3: A plot of the simulation run to calculate  $e_s$  using the binary image of B15b on JD 50 of 2001. The blue line indicates the actual motion of the simulated iceberg, while the red line shows the estimated rotation  $\phi$ . The error bars show the predicted bound  $e_\theta$ . The mean value of  $e_s$  is .0083 radians.

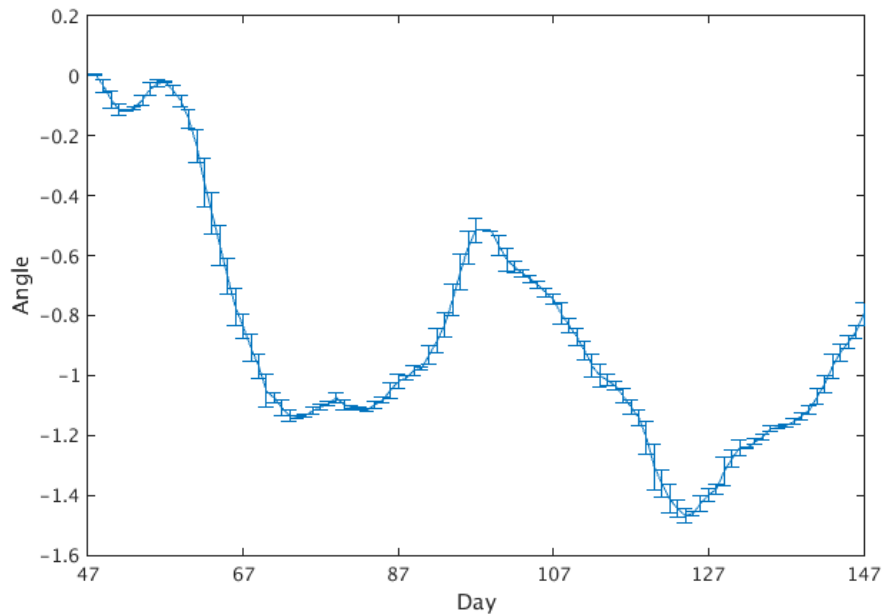


Figure 5.4: A plot of rotational estimates for B15b in radians. This is 100 days of QuikSCAT data from JD 47-147 of 2001, with no melt events. The error bars bound the possible angles for a given day.

## CHAPTER 6. CONCLUSION

### 6.1 Summary

The goal of this thesis is to introduce a new, comprehensive database of iceberg location data. As it stands now, there are multiple available databases of Antarctic iceberg positions. In this thesis I compare and contrast two of these databases: the BYU MERS and NIC databases. As each has advantages and disadvantages, I have made an effort here to consolidate datasets into one comprehensive database, comprised of two sets of files. This allows for easier tracking of icebergs in the future.

Using interpolation and masking methods, more consistent iceberg tracks and information about the surroundings of each iceberg have been included in the second, more derivative database as well. Given that the surroundings of an iceberg affect its movement patterns, this second database gives a single track and the information needed to make accurate predictions of iceberg movement.

Several applications for using the information in the database have been described, including size estimation and rotational motion estimation. Using the methods described, I have independently generated size estimates that fall within 10% of the NIC's reported size estimates, and rotational motion estimates accurate to within .01 rad/day.

Iceberg movement in aggregate can be studied effectively, enabling more sophisticated tracking methodology to be developed. As more icebergs are found and added to the consolidated database, models predicting iceberg behavior can be refined. Behaviors such as movement are more easily tracked and documented with the use of a comprehensive coordinate database. This database allows for easier analysis of the information that has been collected and a deeper understanding of icebergs in the future.

## 6.2 Future Work

While much progress has been made, there is room for additional work. Some suggestions for future work include the following.

### 6.2.1 Melt Event Mitigation

While the size estimation algorithm is accurate for most days of an iceberg's lifetime, it does not provide accurate estimates during melt events. Such melt decrease the contrast between the iceberg's surface  $\sigma^0$  and the ocean. In some cases, this renders the iceberg indistinguishable from its surroundings in  $\sigma^0$  SIR images. Additional research into different methods of utilizing scatterometer data to find a way to distinguish icebergs from sea ice or ocean water could mitigate the error introduced by melt events and create a more generally applicable size estimation algorithm.

### 6.2.2 Automatic Iceberg Location

The method of iceberg size estimation developed in this thesis relies in the input of iceberg positions that have already been determined manually. With additional data on the general  $\sigma^0$  values that an iceberg is likely to take on a certain day, it could be possible to use SIR images to locate icebergs algorithmically by extending the ideas presented in this thesis.

### 6.2.3 Iceberg Location Prediction

The positional data from iceberg tracks can also be used to predict iceberg locations in the future. With the assumption that Antarctic ocean currents do not change much from year to year, it is possible to create a model of ocean currents using the positional data in the new database along with some calculations to determine the speed and direction of travel of any icebergs in a given area. Additional research into the effect of rotation or size on the speed and direction of travel of an iceberg could allow for more accurate modeling of iceberg motion in the future.

## REFERENCES

- [1] Misra, T., and Kumar, A., 2015. “Scatterometer and RISAT-1: ISRO’s contribution to radar remote sensing.” In *2015 IEEE International Geoscience and Remote Sensing Symposium (IGARSS)*, IEEE, pp. 4220–4223. iv, 5
- [2] K. D. Klaes, M. C., et al., 2007. “An introduction to the EUMETSAT polar system.” *Bulletin of the American Meteorological Society*, **88**(7), p. 1085. iv, 6
- [3] , April 2016. Antarctic ice shelf sheds bergs. iv, 14
- [4] F.T. Ulaby, D. L., et al., 2014. *Microwave radar and radiometric remote sensing.*, Vol. 4 University of Michigan Press Ann Arbor. 1, 4, 7
- [5] C.L. Parkinson, J. C., et al., 1987. “Arctic sea ice, 1973-1976: Satellite passive-microwave observations.”. 2
- [6] Remund, Q., and Long, D., 1999. “Sea ice extent mapping using Ku band scatterometer data.” *Journal of Geophysical Research: Oceans*, **104**(C5), pp. 11515–11527. 2
- [7] D.G. Long, M. D., et al., 2001. “Global ice and land climate studies using scatterometer image data.” *Eos, Transactions American Geophysical Union*, **82**(43), pp. 503–503. 4
- [8] W. Tsai, M. S., et al., 2000. “Seawinds on QuikSCAT: sensor description and mission overview.” In *Geoscience and Remote Sensing Symposium, 2000. Proceedings. IGARSS 2000. IEEE 2000 International*, Vol. 3, IEEE, pp. 1021–1023. 4
- [9] F.M. Naderi, M. F., and Long, D., 1991. “Spaceborne radar measurement of wind velocity over the ocean-an overview of the NSCAT scatterometer system.” *Proceedings of the IEEE*, **79**(6), pp. 850–866. 5
- [10] SAF, O., 2013. ASCAT wind product user manual Tech. rep., SAF/OSI/CDOP2/KNMI/TEC/MA/140, available on <http://www.osi-saf.org/biblio/docs/> accessed on 06 February. 6
- [11] D.G. Long, P. H., and Whiting, P., 1993. “Resolution enhancement of spaceborne scatterometer data.” *IEEE Transactions on Geoscience and Remote Sensing*, **31**(3), pp. 700–715. 7
- [12] Early, D., and Long, D., 2001. “Image reconstruction and enhanced resolution imaging from irregular samples.” *Geoscience and Remote Sensing, IEEE Transactions on*, **39**(2), pp. 291–302. 7
- [13] D. L. Naftz, J. R., and Ranville, J., 1991. “Glacial ice composition: A potential long-term record of the chemistry of atmospheric deposition, wind river range, wyoming.” *Water Resources Research*, **27**(6), pp. 1231–1238. 7

- [14] K. M. Stuart, D. G. L., 2011. “Tracking large tabular icebergs using the seawings ku-band microwave scatterometer.” *Deep Sea Research Part II Topical Studies in Oceanography*, **58**(11), pp. 1285–1300. 8
- [15] A. O. Cefarelli, M. V., and Ferrario, M., 2011. “Phytoplankton composition and abundance in relation to free-floating antarctic icebergs.” *Deep-Sea Research II: Topical Studies in Oceanography*, **58**, pp. 1436–1450. 9
- [16] T. Scambos, R. Ross, e. a., 2008. “Calving and ice-shelf break-up processes investigated by proxy: Antarctic tabular iceberg evolution during northward drift.” *Journal of Glaciology*, **54**(187), pp. 179–191. 9
- [17] L. Evers, D. Green, N. Y., and Snellen, M., 2013. “Remote hydroacoustic sensing of large icebergs in the southern indian ocean: Implications for iceberg monitoring.” *Geophysical Research Letters*, **40**, pp. 4694–4699. 9
- [18] J. Tournadre, N. Bouhier, F. G.-A., and Rmy, F., 2015. “Large icebergs characteristics from altimeter waveform analysis.” *Journal of Geophysical Research: Oceans*, **120**, pp. 1954–1974. 9
- [19] D. G. Long, M. R. D., et al., 2001. “Global ice and land climate studies using scatterometer image data.” *Transaction of American Geophysical Union*, **82**(43), p. 503. 11
- [20] Hennig, S., 2013. “Exploring the benefits of active vs. passive spaceborne systems.” *Earth Imaging Journal*, **10**(6). 13
- [21] F. N. Fritsch, R. E. C., 1980. “Monotone piecewise cubic interpolation.” *SIAM J. Numerical Analysis*, **17**, pp. 238–246. 14
- [22] N. S. Baidya, R. N., 2009. “Image thresholding by variational minimax optimization.” *Pattern Recognition*, **42**(5), pp. 843–856. 20
- [23] Mahalanobis, P. C., 1936. “On the generalised distance in statistics.” *Proceedings fhte National Institute of Sciences of India*, **2**(1), pp. 49–55. 21
- [24] A. Savitzky, M. J. E. G., 1964. “Smoothing and differentiation of data by simplified least square procedure.” *Analytic Chemistry*, **36**(8), pp. 1627–1639. 24
- [25] Husseiny, A. A., 1977. *Iceberg Utilization: Proceedings of the First International Conference held at Ames, Iowa*. Iowa State University Research Foundation. 27
- [26] A. W. Fitzgibbon, M. Pilu, R. B. F., 1999. “Direct least squares fitting of ellipses.” *IEEE Trans. PAMI*, **21**, pp. 476–480. 27
- [27] D. Cakmakov, E. C., 2005. “Shape matching of digital curves.” *4th International Symposium on Image and Signal Processing and Analysis*, pp. 457–461. 30

## **APPENDIX A. DATABASE FILE FORMAT DOCUMENTATION**

### **A.1 Introduction**

The purpose of the new consolidated iceberg positional database discussed in this thesis is to provide a consistent data base for scientific research. In this appendix, the overall structure and format of the database are shown. Individual data fields are also described.

### **A.2 Structure**

Included in the database are two sets of data files. The first set is comprised of raw position data, with a section for interpolated data. It is arranged into multiple files, one per iceberg, with each file named for the iceberg it represents. Also included is a single file containing positional data for every iceberg in the database, one after the other, arranged in the same format as the other files.

The second set of data files contains derivative measurements and a high level overview of the positional data. It contains a single track for each iceberg, size and rotation measurements, daily displacement in kilometers, and a flag showing which sensors are used to determine the single track latitude and longitude. These files are arranged similarly to the first set of data files, with a file for each iceberg as well as a single file for all the icebergs contained in the database.

### **A.3 Format**

Each file in the two data sets discussed above is arranged in the same format for ease of use. The files contain headers which describe the type of data contained in the file column. Each row of the file corresponds to a single day in the iceberg's lifetime, with each column containing either a number or flag corresponding to the reported data for that day. Columns are separated by commas. Thus, the files are in the CSV format and can be read by standard spreadsheet programs.

The following subsections describe each of the data fields that a file could contain within the database, with a short description of how the value of the field is derived. The titles of each subsection correspond to the data field name on the first line of the file.

### **A.3.1 Sensors**

Each sensor that contributes to the database has two separate fields. The first is denoted by the name of the sensor followed by ‘\_1’ and contains latitude measurements. The second also has the name of the sensor, followed by ‘\_2’, and contains longitude measurements. Only sensors that contribute measurements for a given iceberg are included in the file for that iceberg.

### **A.3.2 date**

The date corresponding to the measurements of that row, formatted as YYYYDDD, where Y is the four digit year and D is the three digit Julian Day, with leading zeros if needed.

### **A.3.3 size\_1**

Length of the major axis of the iceberg in nautical miles, as reported by the NIC. Values given by the NIC are rounded to the nearest integer.

### **A.3.4 size\_2**

Length of the minor axis of the iceberg in nautical miles, as reported by the NIC. Values given by the NIC are rounded to the nearest integer.

### **A.3.5 area**

An estimate of the area of the iceberg on a given day in  $km^2$ . This value is derived using the algorithm described in Section 4 of this thesis.

### A.3.6 date\_gap

A derivative measurement that describes the number of days between the measurements on one row and the measurements of the row immediately preceding it in the data file. Due to interpolation between most measurements with a date gap, this value is generally 1.

### A.3.7 disp

The displacement in kilometers of the iceberg from the position given on that row and the row before it. Combined with date gap information, this column can be used to find the velocity of an iceberg.

### A.3.8 flags

A hexadecimal number corresponding to the sensors used to create the single track, as well as a single bit to show if the measurement is interpolated. The bits are arranged as follows:

Bit	1-7	8	9	10	11	12	13	14	15	16
Sensor	Unused	SASS	ERS	NSCAT	SeaWinds	QuikSCAT	OSCAT	ASCAT	NIC	Interpolated

For example, the flag '12' corresponds to a measurement using data from QuikSCAT and the NIC, with no interpolation.

### A.3.9 lat

The latitude measurement of the iceberg on a given day in degrees. This value is an aggregate of any sensor measurements for that day, averaged together.

### A.3.10 lon

The longitude measurement of the iceberg on a given day in degrees. This value is an aggregate of any sensor measurements for that day, averaged together.

### A.3.11 mask

The mask number for an iceberg on a given day. This is a number ranging from 0-3 corresponding to the surroundings of the iceberg on that day, as shown in the table below:

Mask	Class
0	Near Land
1	Sea Ice
2	Open Ocean
3	Unknown

### A.3.12 rotation

An estimate of the rotation angle, in radians, from the previous day. This value is derived using the algorithm described in Section 5 of this thesis.